

# Lateral trapping of DNA inside a voltage gated nanopore

Thomas Töws and Peter Reimann

*Fakultät für Physik, Universität Bielefeld, 33615 Bielefeld, Germany*

The translocation of a short DNA fragment through a nanopore is addressed when the perforated membrane contains an embedded electrode. Accurate numerical solutions of the coupled Poisson, Nernst-Planck, and Stokes equations for a realistic, fully three-dimensional setup as well as analytical approximations for a simplified model are worked out. By applying a suitable voltage to the membrane electrode, the DNA can be forced to preferably traverse the pore either along the pore axis or at a small but finite distance from the pore wall.

## I. INTRODUCTION

The detection, analysis, and manipulation of DNA and other macromolecules by means of solid-state nanopores [1, 2] is currently a particularly active branch of nanoscience and -technology [3]. With respect to one of the central objectives in this context, namely DNA sequencing, important breakthroughs have been achieved in recent years, yet a number of key issues are still considered as not satisfactorily resolved [4]. In particular, at relatively weak externally applied driving fields, thermal noise effects are still too large, while at stronger fields the DNA translocates through the pore too quickly to resolve single nucleotides according to their minimally differing current signals [5].

One promising idea to slow down the translocation dynamics is to integrate an electrode into the porous membrane, giving rise to precisely localized and/or time-dependent forces on the DNA in and close to the nanopore. For example, Shankla and Aksimentiev explored in Ref. [6] how the conformation and adhesion of single stranded DNA can be controlled by electrically biasing a graphene membrane. Here, we will specifically focus on embedded membrane electrodes, i.e., they are covered by a thin layer of non-conducting material. Such a “nanopore capacitor” has been experimentally realized for the first time in 2006 by Gracheva et al. to demonstrate the detectability of short DNA fragments [7]. By means of a theoretical multi-scale modeling they furthermore demonstrated that by optimizing (in particular downsizing) the system, even single nucleotides may become detectable. In subsequent works they also investigated various modifications of the original setup by theoretical means [8–11]. Besides the detection, also the possibility of steering the DNA translocation with the help of membrane electrodes was theoretically predicted.

A rather similar experimental system was realized by Yen et al in Ref. [12], reducing the DNA translocation speed by a factor of up to 20 by applying an appropriate gate voltage to the membrane electrode, and thus confirming earlier theoretical predictions in Refs. [13–15]. Solid state nanopores with integrated membrane electrodes were also successfully fabricated by Nam et al. [16] and by Jiang and Stein [17], while Lieber and co-workers realized a DNA sensor, implementing a field effect transistor by means of a nanopore and a narrow

membrane electrode [18].

Systems involving more than one embedded membrane electrodes have been addressed experimentally in Ref. [19] and theoretically in Refs. [10, 20, 21]. In particular, Stolovitzky and co-workers [20, 21] demonstrated by means of molecular dynamics simulations a base-by-base ratcheting motion of single stranded DNA through a solid-state nanopore. However, this model is based on several assumptions which may be difficult to meet in an experiment: the applied gate voltages are very high; the pore is assumed to be infinitely long or to implement periodic boundary conditions; the pulling force on the DNA must be applied via a soft spring, which is indispensable for the ratcheting motion.

In our present work, the main focus is on the lateral forces, i.e. the force components acting upon the DNA during its passage through the pore along the direction perpendicular to the pore axis. In particular, we explore the possibility to control those lateral forces by the voltage which is applied to an embedded membrane electrode. Our analytical and numerical analysis shows that osmotic pressure effects due to the high ion concentrations near the pore wall and the DNA play a particularly prominent role in this context. We show that by suitably choosing the gate voltage, the DNA can be forced to traverse the pore either along the pore axis, or at a small but finite distance from the pore wall or can even be forced to touch the wall. This relatively simple way to control the lateral motion of the DNA opens interesting new possibilities to optimize the detectability and translocation speed of the DNA, or to render the above mentioned ratcheting mechanism easier realizable in an experiment.

The plan of the paper is as follows: In the next section we specify the considered setup, the typical parameter values, our modeling in terms of the coupled Poisson, Nernst-Planck, and Stokes equations, and the potential energy, from which the lateral force derives. In Sect. III we propose a simplified, effectively one-dimensional approximation, which can be treated analytically and admits valuable insights into the main physical mechanisms at work. In Sect. IV an improved, effectively two-dimensional approximation is considered, which can be explored with relatively moderate numerical effort, and can still be quite well explained by means of the one-dimensional model. In Sect. V, the fully

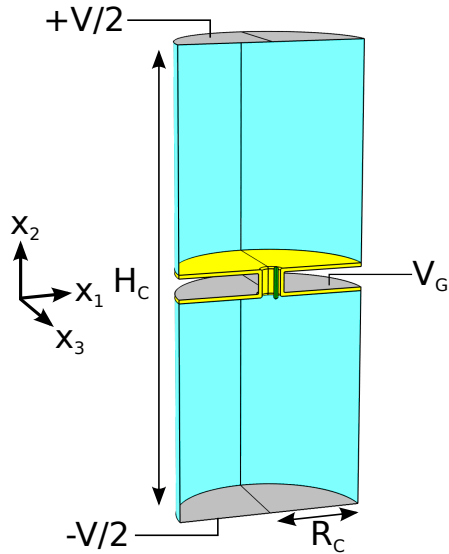


FIG. 1: (Color online) Schematic cross-section through the considered setup. A cylindrical container of height  $H_c$  and radius  $R_c$  is filled with electrolyte solution (blue) and is divided by a membrane. The membrane contains a coated gate electrode, a cylindrical nanopore, and an elongated particle, see also Fig. 2 for a close-up. External voltages  $V/2$ ,  $-V/2$ , and  $V_G$  can be applied to the two electrodes at the top and the bottom of the container, and to the membrane gate electrode, respectively. The origin of the Cartesian coordinates is located at the pore center, but is drawn here off the center for better visibility. The intersection with the  $x_1 = 0$  plane is indicated as thin black line to support the perspective view. The entire sketch is drawn to scale, adopting the standard values from Sect. II A which will be used for the numerical solutions in Sect. V.

three-dimensional problem is numerically tackled, which in turn is found to often be not too far off the two-dimensional approximation. The final section contains our conclusions and the outlook on experimental applications.

## II. MODEL

### A. Considered setup and typical parameter values

As depicted in Figs. 1 and 2, we consider a system consisting of a cylindrical container of height  $H_c$  and radius  $R_c$ , which is divided into two compartments by a membrane of thickness  $T_m$ . The usual values adopted in our calculations below will be  $H_c = 250$  nm,  $R_c = 50$  nm, and  $T_m = 15$  nm. The two compartments are connected by a nanopore and are filled with an electrolyte solution with a bulk ion concentration of  $c_0$ . To keep things as simple as possible, we restrict ourselves to cylindrical pores (radius  $R_p$ ). Other pore shapes lead to similar results but the details become considerably more complicated. Quantitatively, we will focus on  $R_p = 5$  nm, and

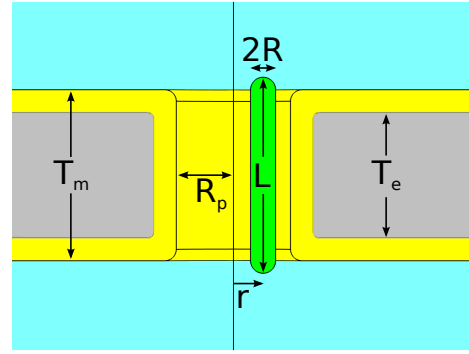


FIG. 2: (Color online) Close-up of the pore region from Fig. 1 (again drawn to scale) with pore radius  $R_p$ , gate electrode (gray) of thickness  $T_e$ , coating (yellow), and total membrane thickness  $T_m$ . The particle (green) of radius  $R$ , length  $L$ , and distance  $r$  from the pore axis (black line) may model, e.g., a DNA segment or an elongated nanoparticle.

on KCl solutions with  $c_0$  in the range of 10 – 100 mM [1, 22–25]. Accordingly, we assume that there are only two relevant charged species ( $i = 1, 2$ ) inside the solution, whose diffusion coefficients  $D_i$  take the known values  $D_1 \simeq D_2 \simeq 2 \cdot 10^{-9} \text{ m}^2/\text{s}$  for  $\text{K}^+$  and  $\text{Cl}^-$  ions in diluted KCl solutions [26]. Here and in the following, we tacitly focus on systems at room temperature.

The membrane is assumed to be a metal electrode of thickness  $T_e$ , coated by a dielectric layer of uniform thickness  $(T_m - T_e)/2$ . In our quantitative examples below, we mainly have in mind an  $\text{Al}_2\text{O}_3$  layer of 2 nm thickness, which is commonly used as membrane or coating material in experiments [17, 27–31]. For such coatings, no electrochemical leakage is experimentally measurable [27, 28], hence we model them as a perfect electrical insulator. As a consequence, the gate electrode does not carry an electric current (embedded electrode). To avoid unrealistically high electric fields at the edges of electrode and membrane, we model them as rounded with radii 0.5 nm and 1 nm, respectively (see Fig. 2).

The permittivity of the membrane coating is denoted as  $\epsilon_m$  and is usually set to the value  $\epsilon_m = 9\epsilon_0$  for  $\text{Al}_2\text{O}_3$  [32], where  $\epsilon_0$  is the vacuum permittivity. The surface charge density of the membrane coating  $\sigma_m$  is caused in the case of  $\text{Al}_2\text{O}_3$  by protonation of the hydroxyl-groups and is approximated as  $\sigma_m = 0.01 \text{ C/m}^2$  [28–31].

Likewise, for the permittivity  $\epsilon_s$  and the viscosity  $\eta$  we will usually choose the standard values  $\epsilon_s = 80\epsilon_0$  and  $\eta = 10^{-3} \text{ Pa}\cdot\text{s}$  for diluted aqueous solutions at room temperature.

As usual in such nanopore systems, an external voltage difference  $V$  can be applied between two “external” electrodes at the top and bottom of the system (see Fig. 1), giving rise to an electrical current through the pore. Without loss of generality, the electrical potential at the top and bottom electrodes are set to  $V/2$  and  $-V/2$ , respectively. Furthermore, a gate voltage  $V_G$  can be applied at the gate electrode.

Finally, we assume that inside the pore there is a cylindrical particle of length  $L$ , radius  $R$ , and spherical end caps. Of foremost interest in our present work will be the situation sketched in Fig. 2, namely when the cylindrical particle is oriented parallel to the pore axis and its center of mass is contained in the central membrane plane but may be off the pore axis by a distance  $r$ . Moreover we restrict ourselves to perfectly stiff and relatively short rods. In particular, our standard value  $L = 17.2$  nm corresponds to the case when the particle length without the end caps coincides with the membrane thickness.

As discussed in Sect. V, longer DNA fragments lead to qualitatively similar results since the main effects are due to the DNA segment inside the pore, and since the persistence length of double stranded DNA (50 nm) is relatively large [15, 33, 34].

Situation when the particle is tilted relatively to the pore axis will be briefly addressed in Appendix IV, the main conclusion being that the parallel alignment is stable against sufficiently small but otherwise arbitrary perturbations of the orientation.

The main example we have in mind is a short fragment of double stranded DNA, exhibiting under typical experimental conditions two electron charges per base pair, which are partially screened, and thus can be modeled in terms of an effective radius  $R = 1.1$  nm and an effective surface charge density  $\sigma_p = -0.05$  C/m<sup>2</sup> [35]. Finally, the permittivity  $\epsilon_p$  of the particle will be set to  $\epsilon_p = 2 \epsilon_0$  [36].

Though the cylindrical particle in Figs. 1, 2 may also model some other kind of macromolecule or nanoparticle, we henceforth often denoted it simply as “DNA”.

## B. Theoretical framework and main observable

The main objective of our present work is to determine the net force which acts in radial direction on the DNA in Fig. 2. For symmetry reasons, the direction of this radial force is trivial (pointing along the connection between pore center and rod center). Moreover, its modulus only depends on the radial distance  $r$  from the pore axis in Fig. 2 and is henceforth denoted as  $F_r(r)$ . This force  $F_r(r)$  and the concomitant potential energy of the DNA in radial direction

$$U(r) := - \int_0^r F_r(r') dr' \quad (1)$$

will be the quantities of foremost interest in our subsequent discussion.

Since the equilibration of the surrounding medium is fast compared to the timescale of DNA motion, we neglect any dynamical back-coupling effects of the DNA motion on the surrounding medium, i.e., we will focus on steady state situations. Furthermore, we will employ the well established continuum approximation based on the coupled Poisson, Nernst-Planck, and Stokes equa-

tions (PNPS) [26, 37–39]: The Poisson equation reads

$$\nabla [\epsilon(\mathbf{x}) \nabla \psi(\mathbf{x})] = -\rho(\mathbf{x}) , \quad (2)$$

where  $\psi(\mathbf{x})$  is the electric potential at  $\mathbf{x} := (x_1, x_2, x_3)$ ,  $\epsilon(\mathbf{x})$  is the permittivity, and  $\rho(\mathbf{x})$  is the charge density due to the fixed surface charges and the mobile ion charges.

Inside the DNA (index  $p$  for “particle”) and inside the membrane coating (index  $m$ ), the Poisson equation (2) reduces to the Laplace equation

$$\epsilon_k \nabla^2 \psi(\mathbf{x}) = 0 , \quad (3)$$

with  $k \in \{p, m\}$  and where  $\epsilon_k$  are the permittivities from Sect. II A.

Denoting by  $c_i(\mathbf{x})$  ( $i = 1, 2$ ) the local concentrations of the two ion species (e.g.  $\text{K}^+$  and  $\text{Cl}^-$ ), and by  $Z_{1,2}$  their valences (usually  $Z_1 = 1$  and  $Z_2 = -1$ ) the total ion charge density amounts to

$$\rho(\mathbf{x}) = N_A e [Z_1 c_1(\mathbf{x}) + Z_2 c_2(\mathbf{x})] , \quad (4)$$

where  $N_A$  is the Avogadro constant and  $e$  the elementary charge. Thus, inside the electrolyte solution (index “ $s$ ”), the Poisson equation (2) takes the form

$$\epsilon_s \nabla^2 \psi(\mathbf{x}) = -N_A e [Z_1 c_1(\mathbf{x}) + Z_2 c_2(\mathbf{x})] , \quad (5)$$

with  $\epsilon_s$  from Sect. II A.

To account for the fixed surface charges, the so far described solutions  $\psi_k(\mathbf{x})$  of the Poisson equation inside the three domains with indices  $k \in \{p, m, s\}$  must satisfy the standard matching conditions

$$[\epsilon_s \nabla \psi_s(\mathbf{x}) - \epsilon_k \nabla \psi_k(\mathbf{x})] \cdot \mathbf{n}(\mathbf{x}) = -\sigma_k , \quad (6)$$

for all  $\mathbf{x}$  on the charged interfaces between “ $s$ ” and “ $k \in \{p, m\}$ ”, where  $\mathbf{n}(\mathbf{x})$  denotes the normal vector pointing into the electrolyte solution, and where  $\sigma_k$  is the surface charge density of the membrane (if  $k = m$ ) or the DNA (if  $k = p$ ) from Sect. II A.

The externally imposed potential difference  $V$  is accounted for via boundary conditions  $\psi(\mathbf{x})|_{S_{1,2}} = \pm V/2$  on the two external electrode surfaces  $S_1$  and  $S_2$  at the top and bottom of the container in Fig. 1. Likewise, the electric potential applied to the gate electrode is taken into account via the boundary condition  $\psi(\mathbf{x})|_{S_3} = V_G$  at the gate electrode surface  $S_3$ , i.e. the interface between the yellow and gray regions in Fig. 2. Finally, we require that the normal component of the electrical field

$$\mathbf{E}(\mathbf{x}) := -\nabla \psi(\mathbf{x}) \quad (7)$$

must vanish at the cylindrical container walls in Fig. 1, that is  $\mathbf{E}(\mathbf{x}) \cdot \mathbf{n}(\mathbf{x}) = 0$ .

The Nernst Planck-equation models the particle current  $\mathbf{J}_i(\mathbf{x})$  associated with the  $i$ -th ion species ( $i = 1, 2$ ), and is given by [26, 37–39]

$$\mathbf{J}_i(\mathbf{x}) = \mathbf{u}(\mathbf{x}) c_i(\mathbf{x}) - D_i \nabla c_i(\mathbf{x}) - \mu_i c_i(\mathbf{x}) \nabla \psi(\mathbf{x}) . \quad (8)$$

The first term on the right hand side describes transport due to convection, with  $\mathbf{u}(\mathbf{x})$  denoting the local fluid velocity. The second term is due to diffusive transport, involving the diffusion coefficients  $D_i$  of the  $i$ -th ion species from Sect. II A. The last term describes the migration of the ions under the influence of the electric field (7), where  $\mu_i := Z_i e D_i / k_B T$  are the ion mobilities,  $k_B$  the Boltzmann constant, and  $T = 293$  K (room temperature). The concomitant steady state continuity equations are

$$\nabla \mathbf{J}_i(\mathbf{x}) = 0, \quad (9)$$

complemented by the following boundary conditions: At the external electrodes (top and bottom of the container in Fig. 1) the ion concentrations  $c_i(\mathbf{x})$  are required to assume the preset bulk value  $c_0$ . On all other fluid boundaries (including the DNA surface) no-flux conditions  $\mathbf{n}(\mathbf{x}) \cdot \mathbf{J}_i(\mathbf{x}) = 0$  are imposed.

Finally, the Navier-Stokes equation is employed in order to determine the fluid flow field  $\mathbf{u}(\mathbf{x})$  and the pressure field  $p(\mathbf{x})$ . Since the Reynolds number is very low under typical experimental conditions, we can safely neglect the inertial term, resulting in the steady state Stokes equation

$$\eta \Delta \mathbf{u}(\mathbf{x}) - \nabla p(\mathbf{x}) - \rho(\mathbf{x}) \nabla \psi(\mathbf{x}) = 0, \quad (10)$$

complemented by the steady state continuity equation for incompressible fluids

$$\nabla \mathbf{u}(\mathbf{x}) = 0, \quad (11)$$

and the following boundary conditions: At the top and bottom electrodes, the pressure is required to assume a preset constant value, which can and will be set to zero, since only pressure gradients actually matter. Furthermore, at the top and bottom electrodes the shear stress (or normal stress)  $H(\mathbf{x})\mathbf{n}(\mathbf{x})$  as well as the tangential fluid flow  $\mathbf{t}(\mathbf{x}) \cdot \mathbf{u}(\mathbf{x})$  must vanish, where  $H$  is the hydrodynamic stress tensor with components  $H_{jk} := \eta(\partial u_j / \partial x_k + \partial u_k / \partial x_j) - \delta_{jk} p$  (arguments  $\mathbf{x}$  omitted and  $j, k = 1, \dots, 3$ ), and where  $\mathbf{t}(\mathbf{x})$  denotes an arbitrary tangential vector. On all other fluid boundaries (including the DNA surface) we impose no-slip boundary conditions  $\mathbf{u}(\mathbf{x}) = \mathbf{0}$ .

Once the above set of equations is solved, the net force  $\mathbf{F}$  acting on the DNA is obtained as the integral

$$\mathbf{F} = \int_S [H(\mathbf{x}) + M(\mathbf{x})] \mathbf{n}(\mathbf{x}) dS \quad (12)$$

over the DNA surface  $S$ . Here,  $H$  is the hydrodynamic stress tensor from above and  $M$  is the Maxwell stress tensor with components  $M_{jk} := \epsilon_s (E_j E_k - \delta_{jk} |\mathbf{E}|^2 / 2)$ , where  $E_j$  are the components of the electrical field from (7) and arguments  $\mathbf{x}$  have been omitted. Finally, the radial force component  $F_r(r)$  and the potential energy  $U(r)$  from Eq. (1) can be readily deduced from the so obtained total forces  $\mathbf{F}$  for various distances  $r$  of the DNA from the pore axis.

### C. Approximations at thermal equilibrium

If  $V = 0$ , the system is at thermal equilibrium, hence all transport currents must vanish. In particular,  $\mathbf{u}(\mathbf{x}) = \mathbf{0}$  and  $\mathbf{J}_i(\mathbf{x}) = \mathbf{0}$  for both ion species  $i = 1, 2$ . The continuity equations (9) and (11) are thus automatically satisfied and from the Nernst-Planck equation (8) one can infer that the concentration fields  $c_i(\mathbf{x})$  are Boltzmann distributed,

$$c_i(\mathbf{x}) = c_0 \exp(-Z_i e \psi(\mathbf{x}) / k_B T). \quad (13)$$

From now on, we restrict ourselves to the most important case with valences

$$Z_1 = -Z_2 = 1, \quad (14)$$

hence the total ion concentration amounts to

$$c_{tot}(\mathbf{x}) := c_1(\mathbf{x}) + c_2(\mathbf{x}) = 2c_0 \cosh(e\psi(\mathbf{x}) / k_B T). \quad (15)$$

Analogously, the Stokes equation (10) yields

$$p(\mathbf{x}) = 2k_B T N_A c_0 [\cosh(e\psi(\mathbf{x}) / k_B T) - 1]. \quad (16)$$

Finally, upon inserting (13) into (5) we recover the Poisson-Boltzmann (PB) equation

$$\epsilon_s \nabla^2 \psi(\mathbf{x}) = 2e N_A c_0 \sinh(e\psi(\mathbf{x}) / k_B T). \quad (17)$$

Taking for granted the approximations  $\cosh(y) \simeq 1 + y^2/2$  and  $\sinh(y) \simeq y$ , Eq. (16) takes the simplified form

$$p(\mathbf{x}) = N_A c_0 (e\psi(\mathbf{x}))^2 / k_B T. \quad (18)$$

and (17) goes over into the Debye-Hückel (DH) equation

$$\nabla^2 \psi(\mathbf{x}) = \lambda_d^{-2} \psi(\mathbf{x}), \quad (19)$$

where  $\lambda_d := \sqrt{\epsilon_s k_B T / 2 N_A c_0 e^2}$  is the characteristic screening length (Debye length). For our usual parameter values mentioned above and  $c_0 = 100$  mM we thus obtain  $\lambda_d \simeq 1$  nm.

Regarding the approximations (18) and (19), two remarks are noteworthy: (i) They will only be exploited in our analytical calculations in Sect. III and Appendix II. Throughout the rest of the paper, we will use the exact Eqs. (16) and (17). (ii) *A priori*, they seem only justified as long as  $|e\psi(\mathbf{x})| \ll k_B T$ . But in practice, they are often observed to still work surprisingly well for  $|e\psi(\mathbf{x})|$  values up to several  $k_B T$  (see e.g. Refs. [39–41]), however, without a truly convincing explanation of this fact being available (a probable cause seems to be an accidental cancellation of errors). The same situation will also be encountered in Sect. III when comparing our analytical approximations with numerically exact solutions.

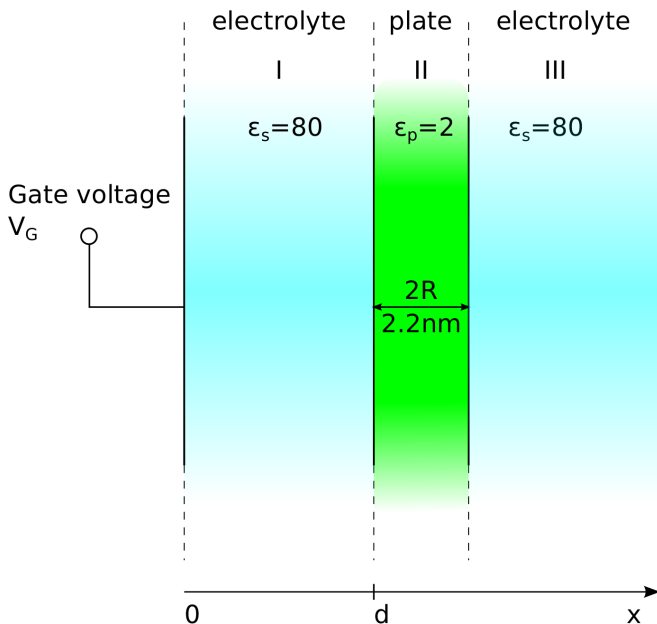


FIG. 3: (Color online) Sketch of the simplified setup considered in Sect. III. A planar gate electrode at  $x = 0$  is subject to a gate voltage  $V_G$  relatively to the reference value  $V = 0$  at  $x = \infty$ . The electrode is coated by an infinitely thin, dielectric (non-conducting) layer with permittivity  $\epsilon_m$  and surface charge density  $\sigma_m$  (omitted in the figure). At a distance  $d$  there is a dielectric plate of thickness  $2R$  parallel to the electrode (region II, permittivity  $\epsilon_p$ ). The gap between electrode and plate (region I) as well as the region beyond the plate (region III) is filled with electrolyte solution (permittivity  $\epsilon_s$ ).

### III. ANALYTICAL APPROXIMATIONS

For the complex geometry from Figs. 1 and 2, we did not succeed to solve the coupled PNPS problem from Sect. II B rigorously by analytical means. To identify the main mechanisms of the interaction between a charged DNA segment and an embedded electrode we will thus reduce the complexity of the original, three-dimensional setup by developing an effectively one-dimensional approximation which can be tackled analytically. In addition, we will compare this approximation with numerical solutions.

#### A. Simplified setup

The setup considered in this section is sketched in Fig. 3. It consists of a dielectric plate of thickness  $2R$  along the  $x$ -axis, of infinite extension along the other two spatial directions (perpendicular to the  $x$ -axis), and with equal surface charge density  $\sigma_p$  on both sides of the plate. Furthermore, there is an infinite planar electrode at position  $x = 0$  with a preset electrical potential  $\psi(x = 0) = V_G$  relatively to the value  $\psi(x) = 0$  at  $x = \infty$ . For convenience, the distance  $d$  between plate and elec-

trode is henceforth denoted as “gap size” and  $V_G$  as “gate voltage”.

The system thus splits up in three regions: Region II represents the dielectric plate. Regions I and III describe a binary electrolyte solution of similar type as in chapter II with a preset “bulk concentration”  $c_0$  at  $x = \infty$ . Likewise, we continue to denote the permittivities in regions I, II, and III as  $\epsilon_s$ ,  $\epsilon_p$ , and  $\epsilon_s$ , respectively. Most other parameters and fields in each of the three regions will be indicated by corresponding indices  $j \in \{I, II, III\}$ .

Finally, we assume that the electrode at  $x = 0$  is covered by an arbitrarily thin, perfectly insulating layer. Closer inspection shows that the solution of the pertinent coupled PNPS problem (see below) becomes independent of the actual permittivity  $\epsilon_m$  and surface charge density  $\sigma_m$  of such an infinitely thin dielectric layer. The intuitive argument is that the freely moving electrons inside the electrode can be thought of as automatically compensating any change in the charge distribution within the infinitely close-by dielectric material. Considering that the electrode potential  $V_G$  remains unchanged, the overall solution of the problem must remain unchanged as well. In other words, the solution of the problem is independent of the detailed charge distribution within the infinitely thin coating and thus independent of  $\epsilon_m$  and  $\sigma_m$ .

#### B. Physical interpretation and simplifications

The setup described above may be viewed as follows: The embedded electrode at  $x = 0$  in Fig. 3 mimics the coated membrane electrode of our original setup from Fig. 2 in the limit of an infinitely large membrane thickness  $T_m$ , an infinitely large pore radius  $R_p$ , and an infinitely thin coating. The dielectric plate in Fig. 3 imitates the DNA segment in Fig. 2 in the limit of an infinite DNA length  $L$ . Moreover, instead of just one single DNA strand we may imagine many identical strands, aligned in parallel and thus approximately amounting to our dielectric plate of thickness  $2R$ .

It seems plausible that with respect to the observable of foremost interest in our present paper, namely the lateral or radial force  $F_r(r)$  acting on the DNA in Fig. 2 (see above Eq. (1)), the situation for one single DNA strand will be different but still comparable to the situation for many DNA strands in parallel. More precisely, the main observable in Fig. 3 will be the force per unit area acting on the infinite plate. The direction of that force is obviously along the  $x$  axis, its magnitude is denoted as  $f(d)$ , and the corresponding potential energy  $U(d)$  is defined similarly as in (1), namely via  $U'(d) = -f(d)$  and  $U(d) \rightarrow 0$  for  $d \rightarrow \infty$  (“pore center”), yielding

$$U(d) = \int_d^\infty dx f(x) . \quad (20)$$

To quantitatively compare those forces  $f(d)$  and  $F_r(r)$  and the corresponding potentials (1) and (20), two quite

natural further steps are needed: (i) Each single DNA strand has a diameter of  $2R$  and the relevant length inside the pore region in Fig. 2 amounts to  $T_m$ . Hence,  $f(d)$  should be multiplied by the “effective DNA area”  $2RT_m$  to extract from the one-dimensional setup in Fig. 3 a force comparable to  $F_r(r)$ . (ii) The distance  $d$  between plate (“DNA”) and electrode (“pore wall”) in Fig. 3 is connected with the distance  $r$  of the DNA from the pore axis in Fig. 2 by the relation  $d = R_p - (r + R)$ , and thus

$$r = R_p - R - d. \quad (21)$$

In the same vein, the above mentioned boundary conditions for the ion concentrations and the electrical potential at  $x = \infty$  seem reasonable approximations to the real situation in Fig. 2 for pores of sufficiently large lengths  $T_m$  and radii  $R_p$ .

For the rest, the transcription of the PNPS equations from (2)-(11) to the present, simplified setup is straightforward and not explicitly carried out here. In particular, the equations governing the three spatial directions decouple from each other, and only those in  $x$ -direction are non-trivial. As a consequence of this decoupling property, the solutions along the  $x$ -direction will be independent from a possibly imposed additional electrical field (or fluid flow) orthogonal to the  $x$ -direction, roughly imitating the effects of the externally imposed voltage  $V$  in Fig. 1.

In other words, we can and will restrict ourselves to solutions along the  $x$ -direction under thermal equilibrium conditions. Since the concomitant one-dimensional version of the PB equation (17) still cannot be analytically solved, we will employ the DH approximation (19). Likewise, the integral (12) still cannot be analytically evaluated in terms of the exact expression (16), hence we will adopt the approximation (18). In order to validate those two approximations, we will furthermore compare the analytics with numerically exact solutions in terms of (17) and (16).

Altogether, our effectively one-dimensional setup from Fig. 3 is expected to reasonably approximate the original, three-dimensional setup from Figs. 1 and 2 if the Debye length  $\lambda_d$  and the gate voltage  $V_G$  remain sufficiently small, and if the distance  $d$  between DNA and electrode is much smaller than the radius  $R_p$  and the length  $T_m$  of the actual pore.

A somewhat similar model, but with two infinitely thick, charged plates, has been previously considered in Ref. [42] in order to study the interaction of two dissimilar particles (one at constant potential and one at constant surface charge density, e.g. to understand the stability of colloids). But our present setup in Fig. 3 with a charged dielectric plate of *finite* thickness has to our knowledge not been worked out before.

### C. Qualitative expectations

For sufficiently large positive or negative gate potentials  $V_G$  in Fig. 3, it is quite plausible that the plate will be attracted to or repelled from the electrode, respectively. Hence, there must exist a “crossover” value of the gate potential  $V_G$ , for which the net force acting on the plate is zero. Furthermore, this crossover potential will generically not be exactly identical for any given gap size  $d$  in Fig. 3 but rather will be some non-trivial function of  $d$ . Likewise, if we consider an arbitrary but fixed gap size  $d_0 > 0$  and set the gate voltage  $V_G$  to the crossover value corresponding to  $d_0$ , then we expect that generically the net force considered as a function of  $d$  changes its sign at  $d = d_0$ .

In other words, we predict that for suitably chosen gate voltages  $V_G$  there must exist a gap size  $d$  at which the total force on the plate vanishes. The natural next question, namely whether this equilibrium position is stable or unstable against small perturbations, cannot be decided anymore by simple intuitive arguments. Later on, we will see that both options may actually be realized, depending on the specific values of all system parameters.

On the qualitative level, these are the main results of our paper. The main remaining goal is to quantitatively confirm these predictions and to extend them to the original, three-dimensional setup from Figs. 1 and 2.

### D. Analytical result and discussion

The analytical approximation announced in Sect. III B is worked out in detail in Appendix II, yielding for the potential energy per unit area from (20) the result

$$U(d) = \frac{1}{\epsilon_s \kappa} \left[ \frac{\gamma^2 \sigma_e^2 - \sigma_p^2}{e^2 \kappa d + \gamma^2} + \frac{\sigma_e \sigma_p}{\gamma \cosh(\kappa d - \ln \gamma)} \right] \quad (22)$$

$$\sigma_e := V_G \epsilon_s \kappa \quad (23)$$

$$\gamma := [1 + \epsilon_p / \epsilon_s \kappa R]^{-1/2}. \quad (24)$$

Here,  $\sigma_e$  from (23) may be viewed as an effective surface charge density of the electrode in the absence of the plate ( $d \rightarrow \infty$ ) [41]. As anticipated at the end of Sect. III A, the above result does not depend on the permittivity  $\epsilon_m$  and the surface charge density  $\sigma_m$  of the infinitely thin coating of the electrode. In the limit  $R \rightarrow \infty$  it follows from (24) that  $\gamma \rightarrow 1$  and one recovers as a special case the result from Ref. [42], describing the interaction of two infinitely thick plates, one with constant potential and one with constant surface charge density.

The approximation (22) represents the main analytical result of our paper. Qualitatively, the discussion of its basic features is straightforward, see Appendix III. Depending on the quantitative values of the two charge densities  $\sigma_e$  and  $\sigma_p$ , one finds that there are four different scenarios of how the function  $U(d)$  may behave within the physically relevant domain  $d \geq 0$ :

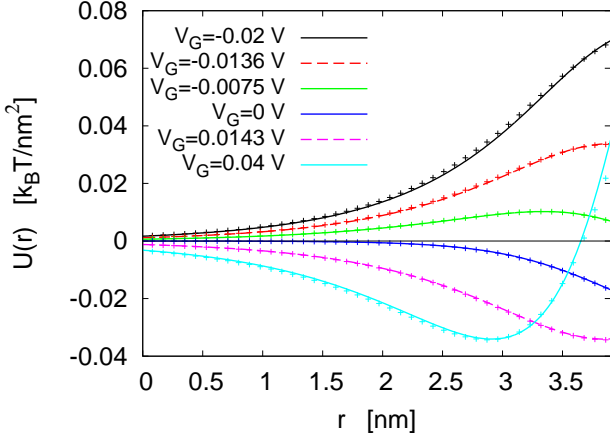


FIG. 4: (Color online) Potential energy per area from (20) versus  $r$  from (21) for the effectively one-dimensional setup from Fig. 3, six different  $V_G$  values as indicated,  $\sigma_p = -0.01 \text{ C/m}^2$ ,  $c_0 = 100 \text{ mM}$ , and all the remaining parameters as specified in Sect. II A. The energy is given in units of thermal energy  $k_B T$  (at room temperature) per surface area (in  $\text{nm}^2$ ) of the dielectric plate in Fig. 3. Lines: Numerically exact solutions. Symbols: Analytical approximation from (22). As detailed in the main text, the variable  $r$  from (21) is adopted for the sake of better comparability with the setups considered later on. Since  $R = 1.1 \text{ nm}$  and  $R_p = 5 \text{ nm}$  (see Sect. II A),  $r$  is restricted to values  $\leq 3.9 \text{ nm}$ , and  $r = 3.9 \text{ nm}$  corresponds to  $d = 0$ , i.e. to the situation where the dielectric plate touches the gate electrode in Fig. 3. The results for  $r < 0$  (i.e. large  $d$ ) are of little interest and have been omitted. The transition from a monotonic to a non-monotonic behavior of  $U(d)$  takes place close to the depicted cases with  $V_G = -0.0136 \text{ V}$  and  $V_G = 0.0143 \text{ V}$ .

If the signs of  $\sigma_e$  and  $\sigma_p$  are equal and  $|\sigma_e| \geq |\sigma_p|$  then  $U(d)$  in (22) is monotonically decreasing. If the signs of  $\sigma_e$  and  $\sigma_p$  are equal and  $|\sigma_e| < |\sigma_p|$  then  $U(d)$  exhibits a local maximum. If the signs of  $\sigma_e$  and  $\sigma_p$  are opposite and  $\gamma^2 |\sigma_e| \leq |\sigma_p|$  then  $U(d)$  is monotonically increasing. If the signs of  $\sigma_e$  and  $\sigma_p$  are opposite and  $\gamma^2 |\sigma_e| > |\sigma_p|$  then  $U(d)$  exhibits a local minimum. Finally, if either  $\sigma_e$  or  $\sigma_p$  is zero then  $U(d)$  is monotonically decreasing or increasing, respectively, and if  $\sigma_e = \sigma_p = 0$  then  $U(d) \equiv 0$ . Typical examples, including the case  $\sigma_e = 0$ , are shown in Figs. 4 and 5.

As repeatedly mentioned, in deriving (22) we have approximated the exact Eqs. (16) and (17) by (18) and (19), respectively. To assess the validity of this approximation, we also included in Figs. 4 and 5 numerical solutions based on the exact Eqs. (17) and (16). As expected, when the gate voltage  $V_G$  and/or the surface charge density  $\sigma_p$  increases (in modulus), the agreement between the exact (numerical) and the approximate (analytical) solutions in Figs. 4 and 5 is seen to deteriorate. On the other hand, and as announced at the end of Sect. II C, the agreement still remains acceptable up to unexpectedly large values of  $|e\psi(\mathbf{x})|/k_B T$  (and thus of

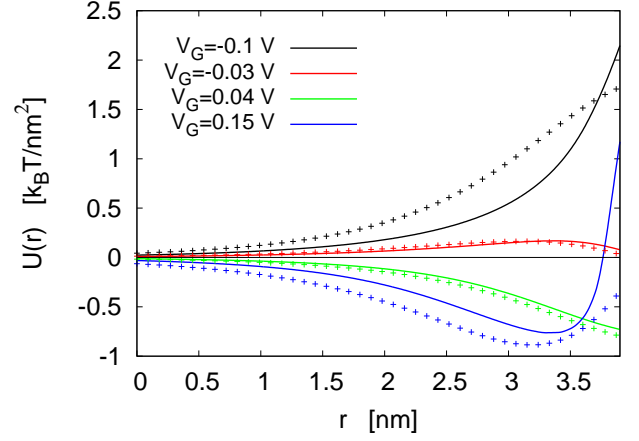


FIG. 5: (Color online) Same as in Fig. 4 but with  $\sigma_p = -0.05 \text{ C/m}^2$  (i.e. the standard surface charge density of our DNA model, see Sect. II A) and modified gate voltages  $V_G$ .

$|eV_G|/k_B T$ ).

Most importantly, the case with  $V_G = 0.15 \text{ V}$  in Fig. 5 provides a first example that our qualitative expectations from Sect. III C may indeed be realized, and may also be quantitatively of interest. Namely, this example indicates that a DNA with an effective surface area of, say,  $10 \text{ nm}^2$  can be trapped at a distance of about  $1 \text{ nm}$  from the “pore wall” with a trapping potential energy of about  $8 k_B T$ , i.e., perturbations by thermal fluctuations are already reasonably weak. Such an effective surface area of  $10 \text{ nm}^2$  may approximately arise for a DNA with radius  $R = 1.1 \text{ nm}$  and a pore length of about  $T_m = 5 \text{ nm}$  in Fig. 2 (see Sect. III B). Also all other parameter values in this example from Fig. 5 are experimentally quite reasonable, see also Sect. II A.

Intuitively, the appearance of such a potential energy minimum as exemplified by Fig. 5 for  $V_G = 0.15 \text{ V}$  can be understood, very roughly speaking, as follows: At very large distances  $d$  in Fig. 3, it is quite plausible that the net force on the dielectric plate will be zero. Moreover, focusing on positive gate voltages  $V_G$  and negative surface charge densities  $\sigma_p$  of the plate, the electric potential  $\psi(x)$  will be positive for  $x = 0$  (namely  $\psi(0) = V_G$ ) and negative for  $x = d$ . As  $d$  decreases, the net force on the plate will change. Likewise,  $\psi(d)$  will change (usually monotonically increase), while  $\psi(0) = V_G$  holds independently of  $d$ . As far as the changes of the force on the plate are concerned, the dominating contribution is due to the net pressure exerted by the electrolyte solution on the surface at  $x = d$  in Fig. 3. This claim may either appear reasonable by itself or can be confirmed by more detailed quantitative considerations, at least for parameter values similar to those in Figs. 4 and 5. This force is proportional to the pressure in Eq. (16) when replacing the argument  $\mathbf{x}$  by  $d$ . As  $d$  decreases,  $\psi(d)$  increases from its initial, negative value to its positive limiting value  $V_G$  when  $d \rightarrow 0$ . Due the hyperbolic co-



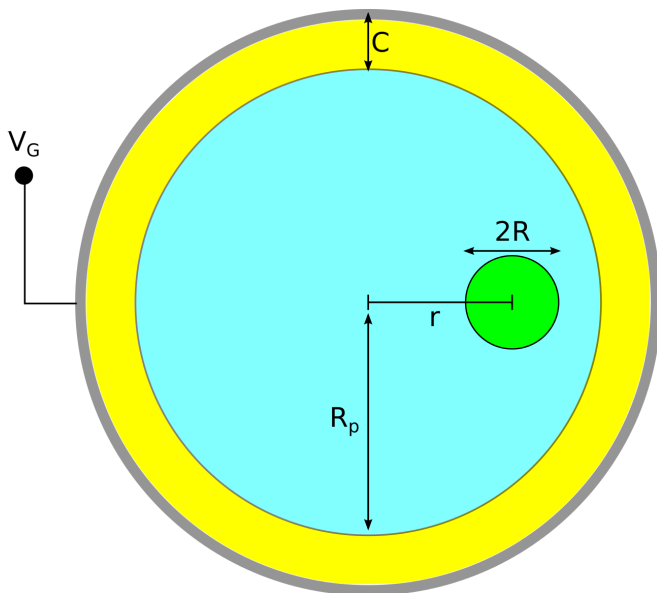


FIG. 6: (Color online) Cross-section through the effectively two-dimensional model, consisting of an infinitely long, cylindrical pore and an infinitely long, rod-shaped DNA of radius  $R$  parallel to the pore axis. Similarly as in Figs. 1 and 2, the electrolyte solution (blue) is confined by a cylindrical gate electrode (gray) with gate voltage  $V_G$  and with a dielectric coating (yellow) of thickness  $C$ , inner radius  $R_p$ , and surface charge density  $\sigma_m$ .

sine on the right hand side of (16), the force on the plate thus first decreases with decreasing  $d$ , reaches its minimum when  $\psi(d) = 0$ , and subsequently increases again. On condition that  $\psi(0) = V_G$  exceeds  $|\psi(d \rightarrow \infty)|$ , the resulting total force on the plate amounts to a repulsion for  $d \rightarrow 0$  and to an attraction for sufficiently large  $d$ , implying the existence of a potential minimum somewhere in between.

Analogous considerations in terms of the ion concentrations  $c_i(d)$  from (13) are straightforward. At large  $d$ , both concentrations approach certain asymptotic values. Upon decreasing  $d$ , one concentration decreases and the other increases, resulting in the quite non-trivial behavior of the total concentration from (15): As  $d$  decreases,  $c_{tot}(d)$  first decreases and later increases again, exactly as for the pressure in (16) (see also Fig. 11 and the discussion in Appendix I). In other words, the behavior of the total pressure variations are governed by the osmotic pressure of the ions.

## IV. TWO-DIMENSIONAL MODEL

### A. Description of the model

The considered setup is depicted in Fig. 6 and essentially amounts to the original model from Figs. 1 and 2 when the pore length  $T_m$  and the particle length  $L$  are

much larger than the pore radius  $R_p$ . In particular, the cylindrical container and the external electrodes in Fig. 1 are now ignored.

The further discussion is analogous to Sect. III B. In particular, the general framework from Sect. II can be readily adapted to our present, translation invariant setup. Furthermore, along the direction perpendicular to the plane from Fig. 6, the pertinent equations and boundary conditions decouple from those in-plane, yielding a steady (or vanishing) motion of the fluid (electro-osmotic flow) and of the DNA, which we can and will ignore from now on. Yet another consequence of this decoupling property is that the equilibrium solutions from Sect. II C are applicable for our subsequent, effectively two-dimensional in-plane explorations.

As before, the observable of main interest is the force  $f(r)$ , acting in radial direction on the DNA per unit length, or equivalently, the potential energy per unit length

$$U(r) := - \int_0^r f(r') dr' . \quad (25)$$

### B. Numerical results

With the exception of a DNA in the pore center, which is of little interest here, an analytical treatment of the problem outlined in Sect. IV A seems impossible. Hence we restrict ourselves to numerical results, obtained along the lines of Appendix I.

Our main focus is on the question to which extent the results for the effectively one-dimensional model from Sect. III carry over to our present, effectively two-dimensional model and to the fully three-dimensional model considered in Sect. V. In a first step, we will thus compare the analytical approximation from chapter III with numerical solutions of the two-dimensional model. In a next step, we will identify particularly promising parameters for the fully three-dimensional explorations in Sect. V.

For a coating of negligibly small thickness  $C$  in Fig. 6, representative numerical results for the potential energy from (25) are depicted in Figs. 7 and 8, and are compared with the analytical approximations from Sect. III D. Considering that the latter approximations are based on an effectively one-dimensional model, the agreement is still quite satisfying. In particular, the existence of the potential minima as well as their depths and positions are reasonably well predicted.

The dashed lines in Fig. 8 indicate that a considerable part of the deviations between the analytics and the numerics is not due to the simplified one-dimensional model *per se*, but rather to the additional approximations on which the analytics is based. A more detailed discussion of the main reasons for the deviations is beyond our present scope.

Numerical results for an experimentally more realistic coating of finite thickness  $C = 2 \text{ nm}$  (see Sect. II A) are



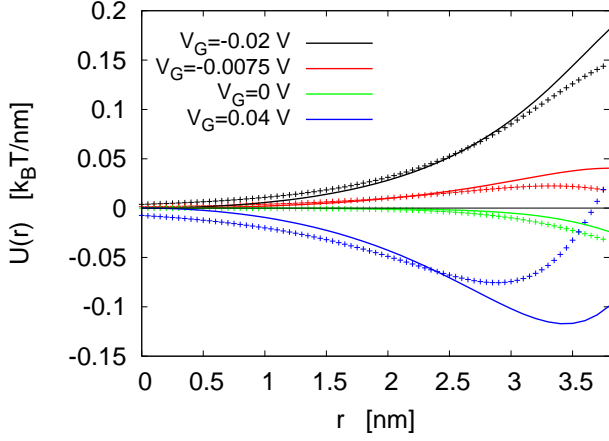


FIG. 7: (Color online) Potential energy per unit length versus  $r$  for the effectively two-dimensional model from Sect. IV A (see also Fig. 6) with  $C = 0$  (infinitely thin coating) and pore radius  $R_p = 5$  nm. All other parameter values are as in Fig. 4 (except that two  $V_G$  values have been omitted in order not to overload the figure). Lines: Numerical solutions. Symbols: Same analytical approximation (22) as in Fig. 4, but multiplied by 2.2 nm to roughly account for the “effective DNA width” in the one-dimensional model, see Sect. IIIB.

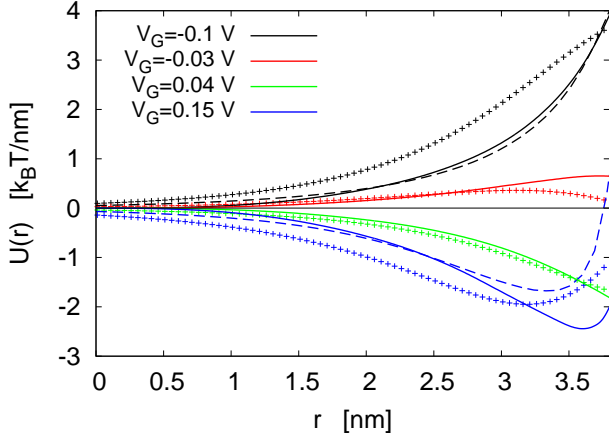


FIG. 8: (Color online) Same as Fig. 7 except that the parameter values are chosen as in Fig. 5. The additional dashed lines for  $V_G = 0.15$  V and  $V_G = -0.1$  V are the numerical solutions from Fig. 5 multiplied by 2.2 nm.

shown in Fig. 9. In order to still obtain potential energy minima with reasonable depths and locations, a bulk concentration of  $c_0 = 10$  mM has been adopted. Compared to all previous numerical examples, the main new feature in Fig. 9 is that potential energies  $U(r)$  which exhibit a local maximum do not seem to exist any more. For the rest, the qualitative behavior is similar as before, but the quantitative details are very different. In particular, analytical approximations are no longer available. On

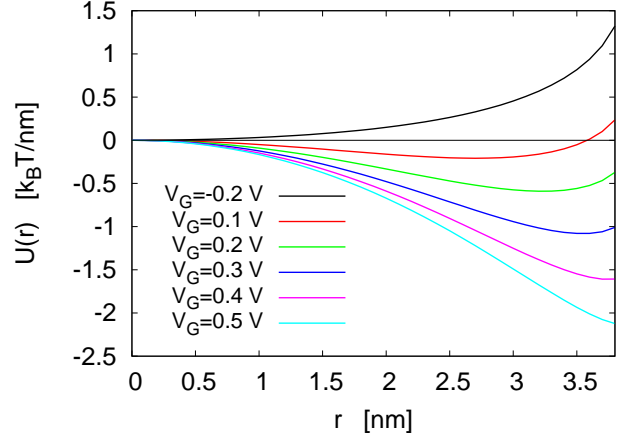


FIG. 9: (Color online) Potential energy per unit length versus  $r$  for the effectively two-dimensional model from Sect. IV A with pore radius  $R_p = 5$  nm, coating thickness  $C = 2$  nm (see Fig. 6), surface charge densities  $\sigma_m = 0.01$  C/m<sup>2</sup> and  $\sigma_p = -0.05$  C/m<sup>2</sup> (see Sect. II A), and bulk concentration  $c_0 = 10$  mM. All other parameter values are as specified in Sect. II A.

the other hand, these solutions amount to a promising starting point for our later, fully three-dimensional explorations.

Analogous to Fig. 9, we also determined the potential energy landscapes for various other parameter values. We desist from presenting further examples and confine ourselves to summarizing some of the main findings when modifying the experimentally most easily variable parameters: The dependence on  $V_G$  is qualitatively similar as in Fig. 9 under most conditions of interest. With increasing pore radius  $R_p$ , the results close to the pore walls ( $r \approx R_p - R$ ) remain essentially as in Fig. 9, but the flat regions near  $r = 0$  become more extended. For substantially smaller pore radii  $R_p$ , things become more involved.

Upon increasing the coating thickness  $C$  and/or the bulk concentration  $c_0$ , the minima of  $U(r)$  (within the region  $0 < r < R_p - R$ ) become less and less pronounced. The latter tendency can be compensated to some extent by increasing the gate voltage  $V_G$  (the compensation is only approximate, and the required  $V_G$  values may become experimentally unfeasible due to dielectric breakdown).

As explained at the end of Sect. III A, the surface charge density  $\sigma_m$  of the coating material becomes irrelevant for asymptotically thin coatings ( $C \rightarrow 0$ ). As  $C$  grows, the dependence on  $\sigma_m$  becomes increasingly strong, but once again, changes of  $\sigma_m$  can be (partially) compensated by adapting the gate voltage  $V_G$ . For instance, to obtain similar potential energy minima as in Fig. 9 for  $\sigma_m = -0.05$  C/m<sup>2</sup>, a gate voltage of about  $V_G = 1.5$  V would be needed. Therefore, a coating material with a positive surface charge, such as Al<sub>2</sub>O<sub>3</sub> with

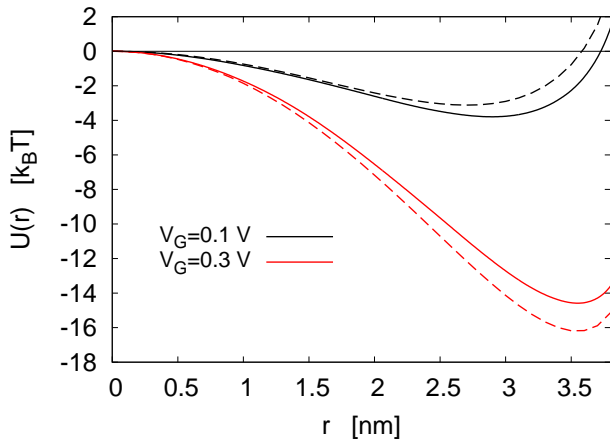


FIG. 10: (Color online) Potential energy  $U(r)$  in units of the thermal energy  $k_B T$  (at room temperature) for two different gate voltages  $V_G$ . Solid: Numerical results for the fully three-dimensional setup, obtained from (1) as detailed in the main text. Dashed: Same as the corresponding two curves in Fig. 9, but multiplied by the pore length  $T_m = 15$  nm to approximately account for the “effective system length” in the two-dimensional model from Sect. IV A.

$\sigma_m = 0.01$  C/m<sup>2</sup> [28–31], may be preferable in an actual experiment.

In accordance with the above observations, it turns out that the intuitive explanation at the end of Sect. III D breaks down as the coating thickness  $C$  increases. The main reason is that the osmotic pressure is no longer dominating the net lateral force on the DNA.

## V. THREE-DIMENSIONAL MODEL

In this Section, we present our numerical findings for the original, fully three-dimensional setup from Figs. 1 and 2 and compare them with the effectively two-dimensional approximation from Sect. IV.

To the best of our knowledge, comparable solutions of the coupled PNPS problem from Sect. II B, including a reasonably sized container as in Fig. 1 and with broken cylinder symmetry as in Fig. 2, have not been previously obtained in the context of DNA translocation through nanopores. More details about the numerics are provided in Appendix I.

Throughout this section, we focus on an experimentally typical external voltage of  $V = 50$  mV (see Fig. 1) and on a bulk concentration of  $c_0 = 10$  mM. All other parameters are as detailed in Sect. II A. In particular: pore radius  $R_p = 5$  nm (see Fig. 2), pore length  $T_m = 15$  nm, thickness of the dielectric coating  $(T_m - T_e)/2 = 2$  nm, coating surface charge density  $\sigma_m = 0.01$  C/m<sup>2</sup>, DNA radius  $R = 1.1$  nm, DNA length  $L = T_m + 2R = 17.2$  nm, and DNA surface charge density  $\sigma_p = -0.05$  C/m<sup>2</sup>, see also the drawn to scale Figs. 1 and 2.

Fig. 10 represents the main result of this section. It shows that the effectively two-dimensional model from Sect. IV approximates the fully three-dimensional situation very well.

In particular, the potential energies  $U(r)$  for other gate voltages  $V_G$  than shown in Fig. 10 behave analogously to those in Fig. 9. It follows that the range of gate voltages covered by Fig. 10 is particularly interesting in that the potential energy  $U(r)$  exhibits reasonably deep (compared to the thermal noise strength  $k_B T$ ) minima, which are located close (but not too close) to the pore wall.

A more detailed analysis of the numerical results reveals that the two-dimensional approximations agree remarkably well with the three-dimensional solutions sufficiently far inside the pore region in Fig. 2 (typical differences are of the order of 1% for  $|x_2| < R_p$ ). As expected, upon approaching the pore ends, the deviations increase and outside the pore the two solutions of course become entirely different. Accordingly, the deviations between the solid and the dashed lines in Fig. 10 are mainly due to the effects near the pore ends. For similar reasons, the externally applied voltage  $V$  plays a rather minor role. E.g., both solid curves in Fig. 10 (obtained for  $V = 50$  mV) change (decrease) by less than  $0.4 k_B T$  in the case  $V = 0$ . Likewise, longer DNA segments lead to quite similar results. E.g., both solid curves in Fig. 10 (obtained for a DNA length of  $L = 17.2$  nm) change (decrease) by less than  $1.5 k_B T$  when choosing  $L = 75$  nm. Finally, the dependence of the lateral forces (and thus of  $U(r)$ ) on the pore length  $T_m$  is, as expected, approximately linear (as long as  $L > T_m$ ), except for rather small  $T_m$ . But the latter regime is anyhow of little interest, since the potential energy minima are then no longer sufficiently deep compared to the perturbations by thermal fluctuations.

The good agreement between the two- and three-dimensional solutions in Fig. 10 also implies that the dependence on further experimentally easily variable parameters remains approximately the same as discussed at the end of Sect. IV B. In particular, upon increasing the bulk ion concentration  $c_0$  one finds that the minima of the potential energy  $U(r)$  become less and less pronounced compared to Fig. 10. To some extent, this tendency can be compensated by reducing the coating thickness  $C$  and/or increasing the gate voltage  $V_G$ , but the experimental feasibility of both options may be quite limited. The only remaining possibility to obtain sufficiently deep potential minima (compared the perturbations by thermal noise) is to work with sufficiently long pores and particles ( $L$  and  $T_m$  in Fig. 2). Yet another consequence of increasing  $c_0$  is that appreciable variations of  $U(r)$  are confined to smaller and smaller neighborhoods of the pore wall (the quite obvious reason is the decreasing Debye screening length of particle and pore). In view of the resulting very small distances between particle and pore wall, one then may question the validity of our continuum approximation (see Sect. II B) and of our neglecting

any chemical and mechanical interactions between particle and wall (adhesion, friction etc.). In conclusion, we expect that the most promising concentrations for our purposes will be relatively small but still doable (experiments working with  $c_0 = 20$  mM are exemplified by Refs. [23–25]).

## VI. CONCLUSIONS

We have demonstrated within a simplified, but still reasonably realistic theoretical model that a DNA fragment in a nanopore can be forced to traverse the pore at a preset distance from the pore wall by means of an embedded (dielectrically coated) membrane electrode, and that this distance can be varied by means of the applied gate voltage.

Quantitatively, Fig. 10 summarizes our main findings, showing that the DNA distance from the pore wall can be controlled up to thermal fluctuations of the order of 1 nm. The pertinent potential energy minima become even more pronounced, and thus the DNA-wall distance can be better controlled, as the pore and DNA lengths are further increased.

Qualitatively, the existence of an extremum of the potential energy  $U(r)$  for properly chosen system parameters can be understood on very general grounds (see Sect. III C). The fact that the extremum may even be a minimum requires more detailed considerations, but can still be intuitively explained as the net effect of the osmotic pressure contributions by the different (negatively and positively charged) ion species (see Sect. III D).

Generally speaking, a passage through the pore which is forced to take place close to the pore wall is expected to exhibit similarities with the translocation close to the center of a considerably smaller pore. In particular, the two critical issues mentioned in the introduction, namely thermal fluctuations and the translocation speed may be considerably reduced. More precisely, a pronounced minimum of the radial potential energy reduces noise effects at least in radial direction and probably also with respect to the orientation relatively to the pore axis (see Appendix IV). Moreover, close to the wall, the electroosmotic drag will be reduced and the hydrodynamic interaction with the wall increased, both tending to reduce the translocation speed. Finally, a reduced and better defined distance to the pore wall will also help to improve the resolution of established detection tools such as ionic current readout [1, 5], nanowire field-effect sensors [18], or graphene nanoribbons [43]. To explore the detailed quantitative implications for a specific setup of the latter type remains as an interesting task for future studies.

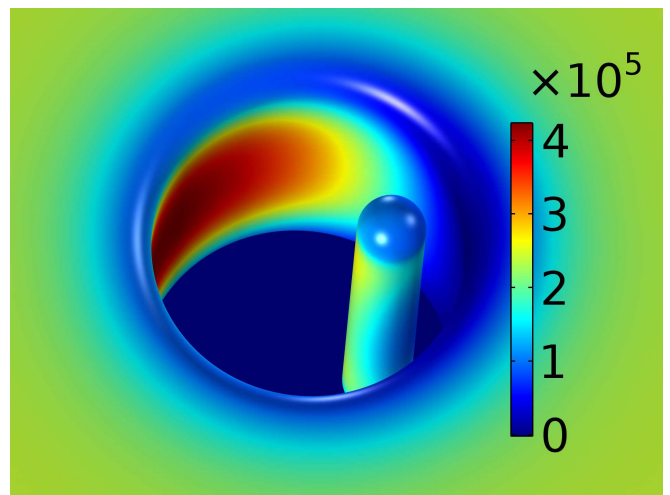


FIG. 11: (Color online) Representative numerical solution of the coupled PNPS problem from Sect. II B for the setup from Figs. 1, 2 and with the standard parameter values as specified in Sect. II A, external voltage  $V = 50$  mV, gate voltage  $V_G = 300$  mV, and bulk concentration  $c_0 = 10$  mM. Depicted is the color coded pressure (in Pa) on the surface of the porous membrane and the rod shaped DNA. More precisely, we plot the excess pressure over the preset value (zero) at the external electrodes in Fig. 1.

## Acknowledgments

This work was supported by Deutsche Forschungsgemeinschaft under RE1344/8-1 and RE1344/9-1, and by the Paderborn Center for Parallel Computing.

## APPENDIX I

In this Appendix, we provide more details of how the numerical results from the main text were obtained and we illustrate how a typical numerical solution looks.

For the complex geometry from Figs. 1 and 2, the numerical solutions of the coupled PNPS problem from Sect. II B were obtained by means of the finite element software COMSOL 5.1. The fully three-dimensional numerical problem still requires a very high number (up to  $2 \cdot 10^7$ ) of degrees of freedom, which is beyond of what is doable on normal office computers. Therefore, we run the program on 4 cores with a memory requirement of up to 620 GB RAM at the Paderborn Center for Parallel Computing.

To illustrate the difficulty of the problem, Fig. 11 exemplifies the numerically obtained behavior of the pressure field  $p(\mathbf{x})$  on the surfaces of the DNA and the membrane. In view of these results it is quite plausible that analytical progress will only be possible by means of considerable approximations (cf. Sect. III).

In fact, the results from Fig. 11 are already quite interesting in themselves and anticipate some key issues of our

more detailed explorations in the main text. Namely, one sees that the net pressure force pushes the DNA towards the pore wall. The main reason is as follows. According to (15) and (16), the pressure is governed by the total concentration of both ion species. Apparently, the two dislike charged surfaces of pore and DNA are mutually expelling their respective screening ions, resulting in an overall reduction of the total ion concentration and hence of the pressure between DNA and near-by pore wall.

## APPENDIX II

In this Appendix we provide the derivation of Eq. (22).

As announced in Sect. IIIB, we will solve the one-dimensional version of the DH equation (19) in regions I and III. Similarly, a one-dimensional Laplace equation like in (3) has to be solved in the remaining region II. Explicitly, these equations read

$$\partial_x^2 \psi_j(x) = \kappa^2 \psi_j(x) \quad \text{for } j=\text{I, III} \quad (26)$$

$$\partial_x^2 \psi_j(x) = 0 \quad \text{for } j=\text{II} . \quad (27)$$

where  $\kappa := \lambda_d^{-1}$  is the inverse of the Debye screening length defined below Eq. (19). Their general solutions are

$$\psi_j(x) = A_j e^{-\kappa x} + B_j e^{\kappa x} \quad \text{for } j=\text{I, III} \quad (28)$$

$$\psi_j(x) = A_j + B_j x \quad \text{for } j=\text{II} , \quad (29)$$

involving six integration constants  $A_j, B_j$ . These constants are fixed by the one-dimensional version of the matching conditions (6) and the boundary conditions  $\psi(x=0) = V_G$  and  $\psi(x \rightarrow \infty) = 0$  from Sect. III A.

For the sake of convenience, we employ the dimensionless variables

$$\hat{x} := \kappa x \quad (30)$$

$$\hat{\psi}(\hat{x}) := \psi(x)/\psi_0 , \quad (31)$$

where the reference potential  $\psi_0$  will be fixed later (see Eq. (41) below).

Due to (30) and (31), Eqs. (28) and (29) can be rewritten in the dimensionless form

$$\hat{\psi}_j(\hat{x}) = \hat{A}_j e^{-\hat{x}} + \hat{B}_j e^{\hat{x}} \quad \text{for } j=\text{I, III} \quad (32)$$

$$\hat{\psi}_j(\hat{x}) = \hat{A}_j + \hat{B}_j \hat{x} \quad \text{for } j=\text{II} \quad (33)$$

with  $\hat{A}_j := A_j/\psi_0$  and  $\hat{B}_j := B_j/\psi_0$ . The corresponding one-dimensional boundary conditions from Sects. II B and III A take the dimensionless form

$$\hat{\psi}_I(0) = V_G/\psi_0 \quad (34)$$

$$\hat{\psi}_{III}(\hat{x} \rightarrow \infty) = 0 \quad (35)$$

$$\hat{\psi}_I(\hat{d}) = \hat{\psi}_{II}(\hat{d}) \quad (36)$$

$$\hat{\psi}_{II}(\hat{d} + 2\hat{R}) = \hat{\psi}_{III}(\hat{d} + 2\hat{R}) \quad (37)$$

$$\epsilon_s \hat{\psi}'_I(\hat{d}) - \epsilon_p \hat{\psi}'_{II}(\hat{d}) = \sigma_p/\kappa\psi_0 \quad (38)$$

$$\epsilon_p \hat{\psi}'_{II}(\hat{d} + 2\hat{R}) - \epsilon_s \hat{\psi}'_{III}(\hat{d} + 2\hat{R}) = \sigma_p/\kappa\psi_0 , \quad (39)$$

where

$$\hat{d} := \kappa d , \quad \hat{R} := \kappa R . \quad (40)$$

Without loss of generality we can choose

$$\psi_0 := \sigma_p/\kappa \quad (41)$$

so that the right hand side of Eqs. (38) and (39) become unity.

Later on, we will see that for the evaluation of the force we only need to determine the constants  $\hat{A}_I, \hat{B}_I$ , and  $\hat{B}_{III}$ . To this end, we introduce (32) into (34), (36), (38) and solve for  $\hat{A}_I$  to obtain

$$\hat{A}_I(\hat{d}) = \frac{V_G e^{\hat{d}} - \frac{1}{\epsilon_s}}{e^{\hat{d}} + \gamma^2 e^{-\hat{d}}} , \quad (42)$$

where  $\gamma$  is defined in Eq. (24) and where the dependence of (42) on  $\hat{d}$  is now explicitly written out for later convenience. Likewise, introducing (42) into (32) and (34) yields

$$\hat{B}_I(\hat{d}) = \frac{\gamma^2 \frac{V_G}{\psi_0} e^{-\hat{d}} + \frac{1}{\epsilon_s}}{e^{\hat{d}} + \gamma^2 e^{-\hat{d}}} . \quad (43)$$

Furthermore, Eqs. (35) and (32) imply

$$\hat{B}_{III} = 0 . \quad (44)$$

Finally, the dimensionful constants are recovered as  $A_I = \psi_0 \hat{A}_I$  and  $B_{I,III} = \psi_0 \hat{B}_{I,III}$ .

Given the electric potential  $\psi(\mathbf{x})$ , the remaining fields readily follow from Eqs. (13), (16), and the text above Eq. (13). Likewise, the resulting force  $f(d)$  on the plate in Fig. 3 can be obtained analogously as in (12), except that  $f(d)$  is now a force per unit area, see Sect. IIIB. Regarding the hydrodynamic stress tensor  $H_{jk}$  (see above Eq. (12)) and the Maxwell stress tensor  $M_{jk}$  (see below Eq. (12)), one finds that

$$H_{11}(x) = -p(x) \quad (45)$$

$$M_{11}(x) = \epsilon_s (E_1^2(x) - E_1^2(x)/2) = \epsilon_s E_1^2(x)/2 \quad (46)$$

and that – due to the one-dimensional nature of the problem and the fact that the velocity field is zero – all other components of  $H_{jk}$  and  $M_{jk}$  vanish. As a consequence, only the force component  $F_1$  in (12) is non-zero. Furthermore, one finds that  $F_1$  can be written as

$$F_1 = [h(d)n_1(d) + h(d+2R)n_1(d+2R)] \Delta S , \quad (47)$$

where  $\Delta S$  denotes the unit surface area element and

$$h(x) := H_{11}(x) + M_{11}(x) . \quad (48)$$

Dividing (47) by  $\Delta S$ , taking into account (45) and (46), and observing that  $n_1(d) = -1$  and  $n_1(d+2R) = 1$  yields for the force per area the result

$$f(d) = f_h(d) + f_{el}(d) \quad (49)$$

$$f_h(d) := p(d) - p(d+2R) \quad (50)$$

$$f_{el}(d) := \frac{\epsilon_s}{2} [\psi_{II}^{\prime 2}(d+2R) - \psi_I^{\prime 2}(d)] . \quad (51)$$

In (51), we exploited that  $\psi'_j(x) = -E_1(x)$  for  $j \in \{I, III\}$ .

A closed analytical expression for the integral in (12) still turns out to be impossible when working on the right hand side of (50) with the exact Eq. (16). Therefore, we invoke its approximation (18), as justified in more detail in Sect. IIIB. Introducing this approximation into (50) and adopting the dimensionless quantities from (30), (31), and (40), we can rewrite (50) and (51) as

$$f_h(d) = \frac{\epsilon_s}{2} \kappa^2 \psi_0^2 \left( \hat{\psi}_I^2(\hat{d}) - \hat{\psi}_{III}^2(\hat{d} + 2\hat{R}) \right) \quad (52)$$

$$f_{el}(d) = \frac{\epsilon_s}{2} \kappa^2 \psi_0^2 \left( \hat{\psi}_{III}^2(\hat{d} + 2\hat{R}) - \hat{\psi}_I^2(\hat{d}) \right). \quad (53)$$

From (44) and (32) we can conclude that

$$\hat{\psi}'_{III}(\hat{x}) = -\hat{\psi}_{III}(\hat{x}). \quad (54)$$

Introducing (52) and (53) into (49) and exploiting (54) yields

$$f(d) = \frac{\epsilon_s}{2} \kappa^2 \psi_0^2 \left( \hat{\psi}_I^2(\hat{d}) - \hat{\psi}_I^2(\hat{d}) \right). \quad (55)$$

By means of (32), (42), and (43) one can rewrite (55) after a short calculation as

$$f(d) = a_0 \hat{A}_I(\hat{d}) \hat{B}_I(\hat{d}) \quad (56)$$

$$a_0 := 2\epsilon_s \kappa^2 \psi_0^2. \quad (57)$$

Exploiting (42) and (43) one readily sees that

$$\hat{A}_I(\hat{d}) \hat{B}_I(\hat{d}) = i_1(\hat{d}) + i_2(\hat{d}) \quad (58)$$

$$i_1(\hat{d}) := \frac{a_1}{(e^{\hat{d}} + \gamma^2 e^{-\hat{d}})^2} \quad (59)$$

$$a_1 := (\gamma V_G / \psi_0)^2 - 1 / \epsilon_s^2 \quad (60)$$

$$i_2(\hat{d}) := a_2 \frac{e^{\hat{d}} - \gamma^2 e^{-\hat{d}}}{(e^{\hat{d}} + \gamma^2 e^{-\hat{d}})^2} \quad (61)$$

$$a_2 := V_G / \epsilon_s \psi_0. \quad (62)$$

The potential energy of the plate at distance  $d$  is given by (20). Observing (56) and (58) it follows that

$$U(d) = a_0 \left( I_1(\hat{d}) + I_2(\hat{d}) \right) \quad (63)$$

$$I_1(\hat{d}) := \kappa^{-1} \int_{\hat{d}}^{\infty} d\hat{x} i_1(\hat{x}) \quad (64)$$

$$I_2(\hat{d}) := \kappa^{-1} \int_{\hat{d}}^{\infty} d\hat{x} i_2(\hat{x}). \quad (65)$$

The integral (64) with integrand (59) can be readily evaluated by substitution:

$$I_1(\hat{d}) = \frac{a_1}{2\kappa} \int_{e^{2\hat{d}} + \gamma^2}^{\infty} \frac{du}{u^2} = \frac{a_1}{2\kappa(e^{2\hat{d}} + \gamma^2)} \quad (66)$$

$$u := e^{2\hat{x}} + \gamma^2. \quad (67)$$

The integrand (61) in the integral (65) can be written as

$$\begin{aligned} I_2(\hat{d}) &= \frac{a_2}{\kappa} \int_{\hat{d}}^{\infty} d\hat{x} \frac{d}{d\hat{x}} \left( \frac{-1}{e^{\hat{x}} + \gamma^2 e^{-\hat{x}}} \right) \\ &= \frac{a_2}{\kappa(e^{\hat{d}} + \gamma^2 e^{-\hat{d}})}. \end{aligned} \quad (68)$$

Inserting (66) and (68) into (63) and exploiting  $\sigma_e = \epsilon_s \kappa V_G$  (see (23)) and (41) results in

$$U(d) = \frac{1}{\epsilon_s \kappa} \left( \frac{\gamma^2 \sigma_e^2 - \sigma_p^2}{e^{2\hat{d}} + \gamma^2} + \frac{2\sigma_e \sigma_p}{e^{\hat{d}} + \gamma^2 e^{-\hat{d}}} \right). \quad (69)$$

Rewriting the numerator of the last term in (69) as  $2\gamma \cosh(\hat{d} - \ln \gamma)$  and substituting  $\hat{d} = \kappa d$  (see (40)) results in formula (22).

### APPENDIX III

In this Appendix, the statements in the third paragraph of Sect. IIID are derived.

In view of (20), the extrema of the function  $U(d)$  from (69) are the solutions of  $f(d) = 0$ . Due to (56) this requires that either  $\hat{A}_I(\hat{d}) = 0$  or  $\hat{B}_I(\hat{d}) = 0$ . Denoting the solutions of the latter two equations as  $\hat{d}_{max}$  and  $\hat{d}_{min}$ , respectively, one can infer from (42), (43) with (23), (41) that

$$\hat{d}_{max} = \ln \left( \frac{\sigma_p}{\sigma_e} \right) \quad (70)$$

$$\hat{d}_{min} = \ln \left( -\frac{\gamma^2 \sigma_e}{\sigma_p} \right). \quad (71)$$

Closer inspection of  $f'(\hat{d})$  shows that  $\hat{d}_{max}$  corresponds (as anticipated by the notation) to a maximum of  $U(d)$  and  $\hat{d}_{min}$  to a minimum.

Since only non-negative  $d$  values are admitted in the model from Sect. III, the left hand side of (70) only counts as a relevant maximum if the argument of the logarithm exceeds unity, and likewise for (71). It follows that  $U(d)$  exhibits a maximum within the domain  $d \geq 0$  if and only if  $\sigma_p / \sigma_e > 0$  and  $|\sigma_e| < |\sigma_p|$ . Likewise,  $U(d)$  exhibits a minimum in the domain  $d \geq 0$  if and only if  $\sigma_p / \sigma_e < 0$  and  $\gamma^2 |\sigma_e| > |\sigma_p|$ . Moreover, if  $\sigma_p / \sigma_e > 0$  and  $|\sigma_e| \geq |\sigma_p|$  then there is a maximum in the domain  $d \leq 0$  (and no further extremum), hence  $U(d)$  is monotonically decreasing in the domain  $d \geq 0$ . Analogously,  $U(d)$  is monotonically increasing for  $d \geq 0$  if  $\sigma_p / \sigma_e < 0$  and  $\gamma^2 |\sigma_e| \geq |\sigma_p|$ . These findings readily imply the statements in the third paragraph of Sect. IIID.

### APPENDIX IV

This Appendix is devoted to stability considerations of the solutions for the three-dimensional setup from Sect. V.

The motion of the idealized, rod-shaped and perfectly stiff DNA segment from Fig. 2 in radial direction is governed by the potential energy  $U(r)$  from (1). According to Fig. 10, for gate voltages between 0.1 V and 0.3 V, the DNA mostly remains in the close vicinity of the potential minimum even in the presence of thermal fluctuations. Perpendicularly to this radial dynamics, there will be a purely diffusive circular motion “around” the pore axis.

So far we always assumed that the DNA in Figs. 1 and 2 is oriented exactly parallel to the pore axis. Next, we address the question how stable this parallel alignment is against small perturbations of the orientation.

We confine ourselves to a simple, qualitative argument along the lines of the well-established, so-called Derjaguin approximation [39]: The starting point is a DNA oriented parallel to the pore axis at a distance  $r$  corresponding to the potential energy minimum. Moreover, we assume that the pore (and the DNA) is relatively long (compared to the pore radius) so that the effectively two-dimensional

approximation from Sect. IV can be safely used. Now, we imagine that the DNA is slightly tilted. Except that the center of mass must be kept fixed and the rotation angles must be small, this reorientation may be chosen arbitrarily. Next, we divide the tilted DNA into still reasonably long, equal pieces, and finally align each piece separately with the pore axis (keeping the center of mass fixed for each piece). It follows that the radial force on each piece is still reasonably well described by the effectively two-dimensional approximation, i.e. each piece experiences a force which tends to drive it into the local minimum of the potential energy. Moreover, the net angular momentum on the DNA can be approximated very well in terms of the radial forces on all pieces. The global energy minimum is reached if and only if all pieces are simultaneously at the potential energy minimum. Elementary geometrical considerations readily show that the latter is only possible if the original DNA was not tilted at all.

- 
- [1] C. Dekker, Nat. Nanotechnol. **2**, 209 (2007).
  - [2] S. J. Heerema and C. Dekker, Nat. Nanotechnol. **11**, 127 (2016).
  - [3] Editorial “The story so far”, Nat. Nanotechnol. **6**, 603 (2011).
  - [4] G. F. Schneider, C. Dekker, Nat. Biotechnol. **30**, 326 (2012).
  - [5] D. Branton et al., Nat. Biotechnol. **26**, 1146 (2008).
  - [6] M. Shankla and A. Aksimentiev, Nat. Commun. **5**, 5171 (2014).
  - [7] M. E. Gracheva, A. Xiong, A. Aksimentiev, K. Schulten, G. Timp, J.-P. Leburton, Nanotechnology **17**, 622 (2006).
  - [8] M. E. Gracheva, A. Aksimentiev, J.-P. Leburton, Nanotechnology **17**, 3160 (2006).
  - [9] G. Sigalov, J. Comer, G. Timp, A. Aksimentiev, Nano Lett. **8**, 56 (2008).
  - [10] D. V. Melnikov, J.-P. Leburton, M. E. Gracheva, Nanotechnology **23**, 255501 (2012).
  - [11] I. A. Jou, D. V. Melnikov, A. Nadtochiy, M. E. Gracheva, Nanotechnology **25**, 145201 (2014).
  - [12] P.-C. Yen, C.-H. Wang, G.-J. Hwang, Y. C. Chou, Rev Sci. Instrum. **83**, 034301 (2012).
  - [13] B. Luan and A. Aksimentiev, J. Phys.: Condens. Matter **22**, 454123 (2010).
  - [14] Y. Ai, J. Liu, B. Zhang, S. Qian, Anal. Chem. **82**, 8217 (2010).
  - [15] Y. He, M. Tsutsui, C. Fan, M. Taniguchi, T. Kawai, ACS Nano **5**, 5509 (2011).
  - [16] S.-W. Nam, M. J. Rooks, K.-B. Kim, S. M. Rossnagel, Nano Lett. **9**, 2044 (2009).
  - [17] Z. Jiang, D. Stein, Phys. Rev. E **83**, 031203 (2011).
  - [18] P. Xie, Q. Xiong, Y. Fang, Q. Qing, C. M. Lieber, Nat. Nanotechnol. **7**, 119 (2012).
  - [19] J. Bai et al., Nanoscale **6**, 8900 (2014).
  - [20] B. Luan, H. Peng, S. Polonsky, S. Rossnagel, G. Stolovitzky, G. Martyna, Phys. Rev. Lett. **104**, 238103 (2010).
  - [21] B. Luan, G. Martyna, G. Stolovitzky, Biophys. J. **101**, 2214 (2011).
  - [22] H. Chang, F. Kosari, G. Andreadakis, M. A. Alam, G. Vasmatzis, and R. Bashir, Nano Lett. **4**, 1551 (2004); A. Aksimentiev, Nanoscale **2**, 468 (2010).
  - [23] A. Spiering, S. Getfert, A. Sischka, P. Reimann, and D. Anselmetti, Nano Lett. **11**, 2978 (2011).
  - [24] S. van Dorp, U. F. Keyser, N. H. Dekker, C. Dekker, and S. G. Lemay, Nat. Phys. **5**, 347 (2009).
  - [25] L. Galla, A. J. Meyer, A. Spiering, A. Sischka, M. Mayer, A. R. Hall, P. Reimann, and D. Anselmetti, Nano Lett. **14**, 4176 (2014).
  - [26] R. F. Probstein, *Physicochemical Hydrodynamics* (Wiley-Interscience, Hoboken, NJ, 2003).
  - [27] Z. Jiang, M. Mihovilovic, J. Chan, and D. Stein, J. Phys.: Condens. Matter **22**, 454114 (2010).
  - [28] B. M. Venkatesan, D. Estrada, S. Banerjee, X. Jin, V. E. Dorgan, M.-H. Bae, N. R. Aluru, E. Pop, and R. Bashir, ACS Nano **6**, 441 (2012).
  - [29] P. Chen, T. Mitsui, D. B. Farmer, J. Golovchenko, R. G. Gordon, and D. Branton, Nano Lett. **4**, 1333 (2004).
  - [30] Y. Liu, and L. Yobas, ACS Nano **10**, 3985 (2016).
  - [31] B. M. Venkatesan, A. B. Shah, J.-M. Zuo, and R. Bashir, Adv. Funct. Mater. **20**, 1266 (2010).
  - [32] J. Robertson, Rep. Prog. Phys. **69**, 327 (2006).
  - [33] S. W. Kowalczyk, D. B. Wells, A. Aksimentiev, and C. Dekker, Nano Lett. **12**, 1038 (2012).
  - [34] S. Kesselheim, M. Sega, and C. Holm, Comput. Phys. Commun. **182**, 33 (2011); Soft Matter **8**, 9480 (2012).
  - [35] S. Getfert, T. Töws, and P. Reimann, Phys. Rev. E **87**, 062710 (2013).
  - [36] S. Buyukdagli, Phys. Rev. E **95**, 022502 (2017); M. Zhang, L.-H. Yeh, S. Qian, J.-P. Hsu, and S. W. Joo, J. Phys. Chem. C **116**, 4793 (2012); B. Jayaram, K. A. Sharp, and B. Honig, Biopolymers **28**, 975 (1989).
  - [37] R. S. Eisenberg, J. Membr. Biol. **150**, 1 (1996).
  - [38] B. Corry, S. Kuyucak, and S.-H. Chung, Biophys. J. **78**, 2364 (2000).
  - [39] J. H. Masliyah and S. Bhattacharjee, *Electrokinetic and Colloidal Transport Phenomena* (Wiley, NJ, 2006); R. L. Panton, *Incompressible Flow* (Wiley, NJ, 2005).



- [40] R. J. Hunter, *Foundations of colloid science*, Oxford University Press, New York, (2001).
- [41] H. Ohshima, *Biophysical Chemistry of Biointerfaces* (John Wiley&Sons, Hoboken, NJ, 2011).
- [42] G. Kar, S. Chander, and T.S. Mika, J. Colloid Interf. Sci. **44**, 347 (1973).
- [43] F. Traversi C. Raillon, S. M. Benameur, K. Liu, S. Khlybov, M. Tosun, D. Krasnozhan, A. Kis, and A. Radenovicet, Nat. Nanotechnol. **8**, 939 (2013).